Available online at www.sciencedirect.com
ScienceDirect
Trans. Nonferrous Met. Soc. China 35(2025) 3030−3042
Transactions of Nonferrous Metals Society of China
www.tnmsc.cn

Non-destructive measurement of Young's modulus for intermetallic compound phase through Brillouin light scattering

Peng PENG[1], Lin LIU[2], Lu GAN[3], Yang-xin YU[1], Yuan-li XU[1], Xu-dong ZHANG[1], Zhi-kun MA[1], Guo-zhi CHAI[4]

1. School of Materials and Energy, Lanzhou University, Lanzhou 730000, China;
2. State Key Laboratory of Solidification Processing, Northwestern Polytechnical University, Xi'an 710072, China;
3. Lanzhou Jinchuan Technology Park Co., Ltd., Lanzhou 730101, China;
4. School of Physical Science and Technology, Lanzhou University, Lanzhou 730000, China

Received 3 January 2024; accepted 2 September 2024

Abstract: Different from the current measurement methods for Young's modulus of metal materials, the Young's modulus of intermetallic compounds (IMCs) was obtained by a non-destructive method based on Brillouin light scattering (BLS) in this paper. The single-phase regions of CoSn, $CoSn_2$, Cu_3Sn and Cu_6Sn_5 phases required for BLS test were obtained by applying long-term thermal stabilization through adjusting temperature gradient. The volume fractions of the corresponding phases near the solid−liquid interfaces of the samples were 98.3%, 94.2%, 99.6% and 95.9%, respectively. All the independent elastic coefficients and Young's moduli of IMCs were obtained by Brillouin scatterometer. The Young's moduli of CoSn, $CoSn_2$ and Cu_3Sn and Cu_6Sn_5 phases obtained through the present method are 115.0, 101.7, 129.9 and 125.6 GPa, respectively, which are in a good agreement with the previous experimental results. Thus, the effectiveness of BLS in measuring the Young's moduli of IMCs in bulk alloys is confirmed.

Key words: Brillouin light scattering; intermetallic compound; elastic stiffness tensor; thermal stabilization; Young's modulus

1 Introduction

The intermetallic compounds (IMCs) are frequently observed in different alloy systems in addition to solid solution phases. IMCs usually have lower solid solubility and higher melting entropy than the latter due to their different atom bonding and structures [1], giving them a high modulus, high hardness, and low ductility [2−4]. Because IMCs have broad industrial application prospects, it is necessary to precisely measure their mechanical properties, including their Young's moduli [5]. The stress−strain curves obtained from tensile tests are employed to calculate Young's moduli of metallic materials [6], but tensile tests require large sample sizes and destroy the sample. In addition, tensile test results are also greatly influenced by sample defects, and cannot be used for IMCs with very low ductility [7,8]. Nano-indentation is also frequently used method [9,10] and causes less damage to the sample than a tensile test. Nevertheless, it leads to different degrees of plastic-deformation strengthening of the sample during loading, which affects the accuracy of the results [11]. Therefore, it is necessary to find a non-destructive approach to measure the Young's modulus without damaging materials.

Brillouin light scattering (BLS) is the inelastic light scattering of light by phonons (elastic waves)

Corresponding author: Peng PENG, Tel: +86-931-8915855, E-mail: pengp@lzu.edu.cn;
Guo-zhi CHAI, Tel: +86-931-8912718, E-mail: chaigzh@lzu.edu.cn
https://doi.org/10.1016/S1003-6326(25)66864-6

or magnons (spin waves), which are generated during the elementary excitation [12]. The quasi-particles discussed in this paper are acoustic phonons. As a non-destructive optical detection technology, BLS can be used to test samples without mechanical contact, providing an important technical means for studying the elastic properties of crystals [13]. The independent elastic coefficients of anisotropic materials can be determined by BLS, from which the Young's modulus can be calculated [14,15]. Due to the limited contrast of early spectrometers, the test objects of BLS were limited to transparent materials [16,17]. For bulk metallic materials, only the BLS spectra of pure copper, aluminum, and iron have been measured so far [18]. Although a single study [18] focused on the Young's modulus of phases with simple cubic structures, it showed that it was possible to expand the applications of BLS to investigate the Young's moduli of other phases. In this paper, BLS was used to non-destructively measure the Young's modulus of intermetallic compound phases. This method avoided plastic deformation caused by accumulation/ subsidence around an indentation when an indenter contacts a sample, thus increasing the measurement accuracy.

To improve the accuracy of the BLS test results, the selection of the preparation process is particularly important, especially for preparing single-phase bulk alloys. Magnetron sputtering, molecular beam epitaxy, and chemical vapor deposition [19−21] are commonly used to prepare low-dimensional materials in the single-phase zone, but it is difficult to obtain single phases in bulk alloys using these methods. Thermal stabilization is commonly carried out before the directional solidification to obtain a homogeneous melt concentration [20−26]. Due to temperature gradient zone melting (TGZM) [27−33] imposed by the temperature gradient, the volume fractions of the liquid phase in the mushy zones, which correspond to the solidification interval of the alloys according to the phase diagrams of the alloys, decrease as thermal stabilization occurs [23−27,30−34]. The successful preparation of single solid phases from the mushy zone through thermal stabilization has been confirmed [35], demonstrating its effectiveness for preparing single-phase bulk alloys.

In this work, two different single-solid-phase peritectic alloys, ($L+\alpha\rightarrow\beta$): Sn−Co (L+CoSn→$CoSn_2$) and Sn−Cu (L+Cu_3Sn→Cu_6Sn_5), were prepared and then analyzed using BLS to calculate their Young's moduli. Both the primary and peritectic phases in these alloys were IMCs [36,37]. The single-phase zones of these IMCs were obtained through a long-term thermal stabilization method. The Young's moduli of the IMCs by the BLS test were in excellent agreement with the results by other methods, demonstrating the validity of using BLS to obtain the Young's moduli of IMCs in alloys.

2 Basic theory of BLS

In the 1970s and 1980s, SANDERCOCK et al [38,39] investigated a double-pass stable scanning interferometer and the triple-pass series Fabry-Perot interferometer, respectively. These experiments demonstrated the feasibility of Brillouin scattering on non-transparent materials. At the beginning of the 20th century, SANDERCOCK [40] experimentally demonstrated the wide application of Brillouin scattering in opaque materials. BLS uses inelastic phonon−phonon scattering to obtain the frequency of the elastic waves by detecting the intensity of scattered light at different frequencies [41,42]. Figure 1 shows a schematic diagram of a typical BLS with a 180° backscattering geometry. The process by which BLS receives and analyzes scattering light is as follows. The Torus 532 laser emits a vertically polarized beam, which is converted into two beams through a beam splitter. One beam is directly received as a reference light by the Fabry-Pérot interferometer (FPI). The other is focused and is obliquely incident on the sample surface. Then, the 180° backscattered light is received by the same lens and focused on the FPI for analysis. Finally, the scattered light signal is detected by a silicon avalanche diode photon counter composed of 1024 channels and transmitted to the data acquisition system for analysis. A series of BLS spectra can be scanned by changing the sample position and incident angle to change the wave vector. The typical error of frequency measurements can be reduced to 1%−2%.

By changing the thickness of the sample, the incident angle, and polarization conditions, the acoustic phonons that can be detected by the BLS spectra are mainly divided into two categories [43]. The first category is the bulk acoustic waves (BAW)

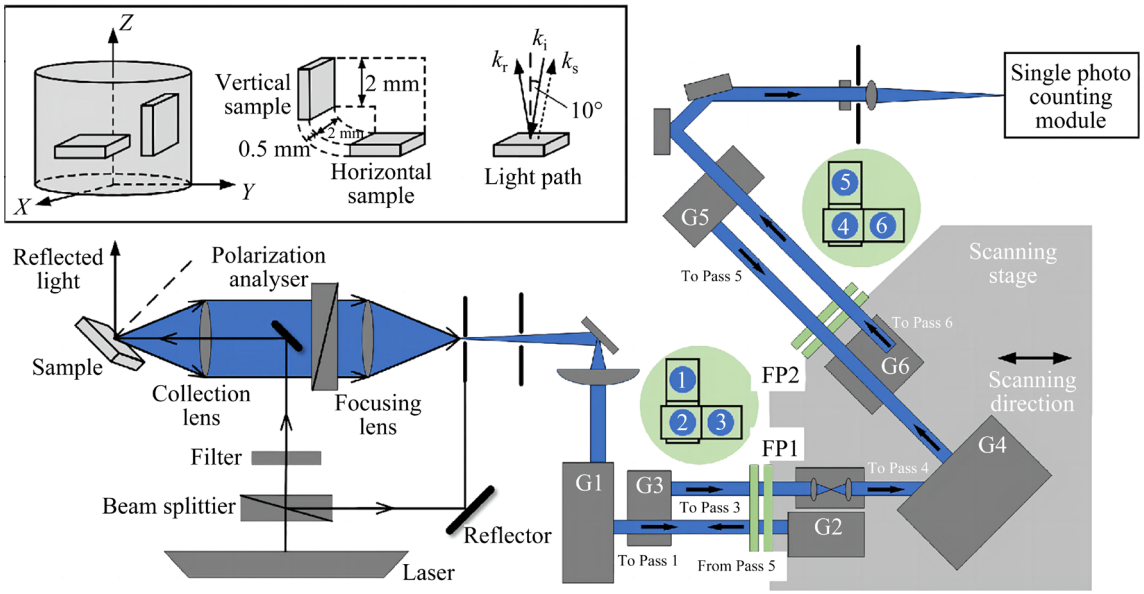

Fig. 1 Schematic diagram of BLS with 180° backscattering geometry (The two parallel green rectangles FP1 and FP2 represent the Fabry-Pérot interferometer)

propagating within a material, including the longitudinal acoustic wave (L) along the vibration propagation direction, and transverse acoustic wave (T) perpendicular to the vibration propagation direction. The second category is surface acoustic waves propagating on the surface, which are Rayleigh surface acoustic waves (RSAWs) [44]. BLS is often used to measure the sound velocity of some films and glasses to obtain their mechanical properties such as independent elastic coefficient (C) and Young's modulus (E) [45]. The independent elastic coefficient is an important parameter that establishes the relationship between sound velocity and Young's modulus. The value of independent elastic coefficients is closely related to the crystal structure, and Hooke's law can be used to describe the relationship between stress and elastic strain [46]. According to Hooke's law:

$$\boldsymbol{\sigma}_{ij}=\boldsymbol{C}_{ijkl}\boldsymbol{\varepsilon}_{kl} \quad (1)$$

where $\boldsymbol{\sigma}_{ij}$ is the second-order stress tensor, $\boldsymbol{C}_{ijkl}$ is the fourth-order elastic coefficient tensor, and $\boldsymbol{\varepsilon}_{kl}$ is the second-order strain tensor. Because the elastic coefficient is symmetric in the tensor matrix, it is expressed by $\boldsymbol{C}_{ij}$.

3 Experimental

The Sn−9at.%Co (Sb−9Co) and Sn−50at.%Cu (Sn−50Cu) alloys were fabricated by melting pure Co, Cu, and Sn (99.9 wt.%) in a vacuum induction melting furnace (VIM−600 M). Samples with a diameter of 6 mm and a length of 110 mm were obtained by wire electrical discharge machining. The TGZM process was carried out in a Bridgman furnace with thermal stabilization time of 6 and 80 h for Sn−9Co alloys and 4 and 45 h for Sn−50Cu alloys. The theoretical predictions of the time required to form the single-phase zones were: t_{Sn-9Co}=77.4 h, and $t_{Sn-50Cu}$=44.6 h. The theoretical calculations are shown in the Supplementary Materials. The temperature was 1273 K during thermal stabilization. When the required time was reached, the samples were quickly quenched in liquid Ga−In−Sn alloy and then cut and polished. The microstructure and phase compositions of the samples were analyzed by an X-ray diffractometer (XRD, Rigaku D/MAX−2400) and a scanning electron microscope (SEM, Apreo-S) equipped with energy-dispersive X-ray spectroscopy (EDS). The volume fraction of the phases was estimated from the transverse sections of samples.

The high-temperature regions of both the primary and peritectic mushy zones of the Sn−9Co and Sn−50Cu alloy samples were cut to prepare horizontal and vertical slices with dimensions of 2 mm × 2 mm × 0.5 mm. The surfaces of the samples were polished to reduce the diffuse scattering of the laser light and obtain a stronger optical signal. The refractive indexes of

intermetallic compounds Cu_3Sn and Cu_6Sn_5 were measured by ellipsometry. Then, the samples were tested using a Brillouin scatterometer with a tandem six-channel (3+3) Sandercock-type Fabry-Pérot interferometer. Because alloys are often opaque, lasers cannot transmit through the materials. Therefore, the best option is to use the back-scattering light path. A schematic diagram of the light path in the backscatter configuration is shown in the inset of Fig. 1, where k_i is the incident light with an incident angle of 10°, k_r is the light reflected from the sample surface, and k_s is the scattered light. The incident light k_i was focused through the lens onto the sample surface, and the scattered light k_s was collected by the lens along the opposite light path as k_i. The same incident wavelength and angle were used for the CoSn, $CoSn_2$, Cu_3Sn, and Cu_6Sn_5 single-phase bulk samples. The laser with a wavelength of 532 nm was used as the incident light, and a polarizer was used to horizontally polarize the light. The vertical polarization of the laser was *P*, and the horizontal polarization of the laser was *S* for phonon tests using BLS. In this work, the incident light with horizontal polarization was incident on the surface of the sample, and then the scattered light with vertical polarization was collected, denoted as PP. In addition, the Brillouin spectra collection time was 6 h for all samples.

4 Results and discussion

4.1 Microstructural evolution

4.1.1 Evolution of mushy zone

To accurately measure the sound velocity in the IMCs to obtain the independent elastic coefficient and Young's modulus of each phase, it is necessary to prepare a complete single-phase zone for the BLS test. During the experiment, we must also consider the extended uncertainty of Brillouin scattering displacement frequency to more accurately evaluate the material parameter values [47]. As mentioned above, obtaining a single-phase by magnetron sputtering or molecular beam epitaxy is much more difficult for bulk alloys than for low-dimensional materials such as membranes. In recent years, the thermal stabilization method has been adopted to obtain single-phase bulk alloys. To prepare single-phase IMC samples, thermal stabilization experiments were carried out at different durations. The overall images of both alloys after different thermal stabilization time are presented in Figs. 2(a−d). In Fig. 2, the samples can be divided into four different zones, wherein the primary mushy zone (Liquid (*L*)+α) and peritectic mushy zone (*L*+β) are located between the complete liquid zone and the solid zone. For the Sn−9Co alloy, the (*L*+CoSn) and the (*L*+$CoSn_2$) zones are observed, while the (*L*+Cu_3Sn) and (*L*+Cu_6Sn_5) zones are observed in the Sn−50Cu alloy. The formation of these different zones was attributed to the temperature gradient imposed during thermal stabilization [23−33]. By referring to the phase diagrams of the alloys, different phases exist at different temperature intervals of the alloys, so different zones with different phase constitutions were formed [24,25,27,30−33].

Figures 2(e−h) show enlarged views of the mushy zone/complete liquid zone interfaces in Figs. 2(a−d), respectively. Similarly, the enlarged views of the mushy zone interface that divides the primary and peritectic mushy zones in Figs. 2(a−d) are exhibited in Figs. 2(i−l), respectively. The decrease in the volume fraction of the liquid phase in the mushy zones upon increasing the thermal stabilization time can be explained by temperature gradient zone melting (TGZM) [24,25,27,30−33]. By referencing the phase diagram of these alloys, the concentration gradient will be established in the liquid droplet during thermal stabilization, resulting in solute (Sn) diffusion from low to high temperatures. Then, the solid phase contacting the liquid phase at the higher temperature is melted, while the liquid phase at the lower temperature solidifies [26,27,30−33]. Consequently, the liquid droplets in the mushy zone gradually move up until they enter the complete liquid phase zone, resulting in a decrease in the liquid phase in the mushy zone. Finally, when the thermal stabilization time is sufficiently long, single-phase zones are formed [23].

4.1.2 Volume fraction of IMCs in mushy zones

To analyze changes in the volume fractions of the IMCs in the mushy zones after long-term thermal stabilization, the volume fractions of the IMCs in different mushy zones of both alloys were measured. Figure 3 shows that the volume fractions of different IMCs in the mushy zone at different positions increased along the height of the mushy zones (*X*). Furthermore, the volume fractions of the

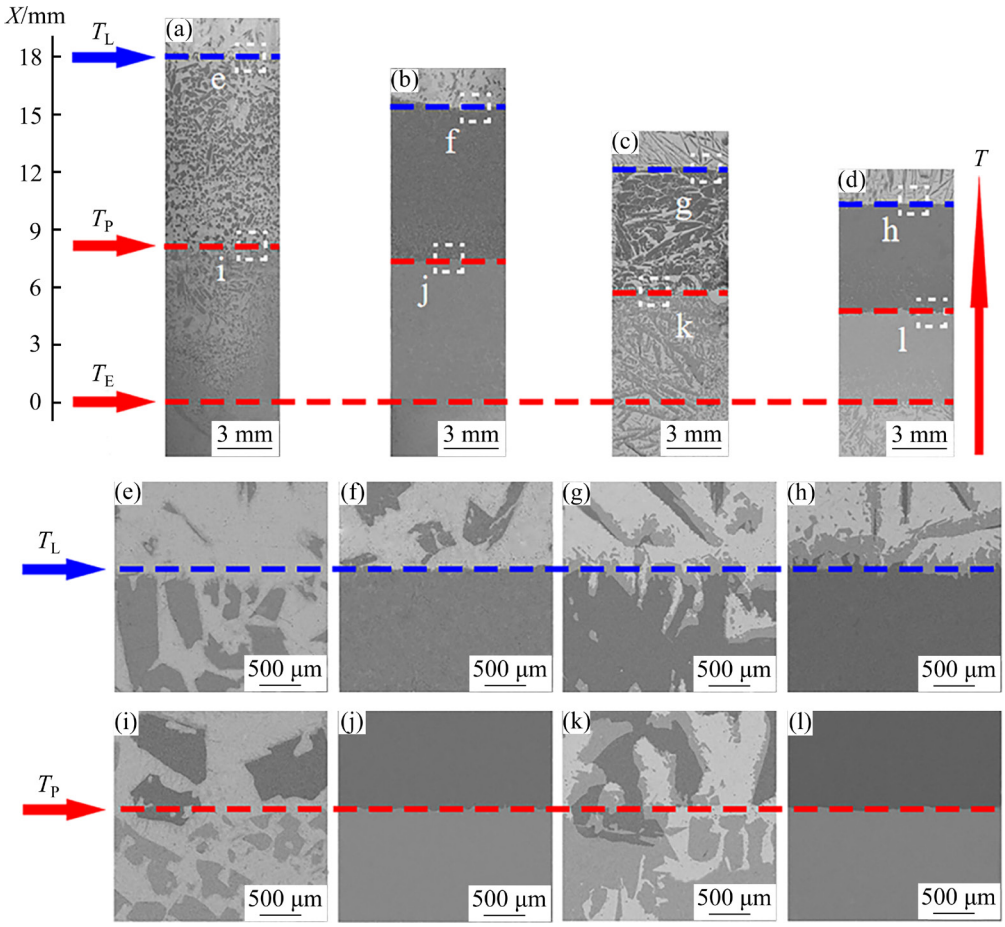

Fig. 2 Microstructures of alloys after different thermal stabilization time: (a, b) Overall images of Sn−9Co alloy after thermal stabilization for 6 and 80 h, respectively; (c, d) Overall images of Sn−50Cu alloy after thermal stabilization for 4 and 45 h, respectively; (e−h) Magnified views of mushy zone/complete liquid zone interfaces in (a−d), respectively; (i−l) Magnified views of two mushy zone interfaces in (a−d), respectively (X is growth distance; T_L is liquidus temperature; T_P is peritectic transformation temperature; T_E is eutectic transformation temperature)

IMCs in the Sn−9Co and Sn−50Cu alloy samples after thermal stabilization for 80 and 45 h were larger than those of the samples at 6 and 4 h at the same position (X). As the position approached the solid−liquid interface, the volume fractions of $CoSn_2$, CoSn, Cu_6Sn_5, and Cu_3Sn phases in the mushy zones reached 94.2%, 98.3%, 95.9%, and 99.6% respectively after long-term thermal stabilization.

4.1.3 XRD analysis results

To determine whether complete single-phase zones were formed after long-term thermal stabilization, the high-temperature regions of primary and peritectic phase mushy zones of the Sn−9Co and Sn−50Cu alloys were examined by XRD. In Figs. 4(a−d), only the peaks of the CoSn, $CoSn_2$, Cu_3Sn, and Cu_6Sn_5 phases were detected, respectively. Therefore, the volume fraction of the liquid phase in these mushy zones was very low, and only these IMCs were in these zones after a sufficient thermal stabilization time. This demonstrates the formation of complete single-phase zones in the high-temperature region of the mushy zones.

4.2 BLS experimental results

BLS tests were performed on vertical (V) and horizontal (H) samples in these four complete single-phase zones to detect the surface waves of IMCs. The results were then used to analyze the mechanical properties of different IMCs. The frequency shift of the incident light after inelastic scattering was obtained by analyzing the Brillouin spectra in BLS experiments. The sound velocity of different surface waves was calculated from the frequency shift and related parameters, and then the

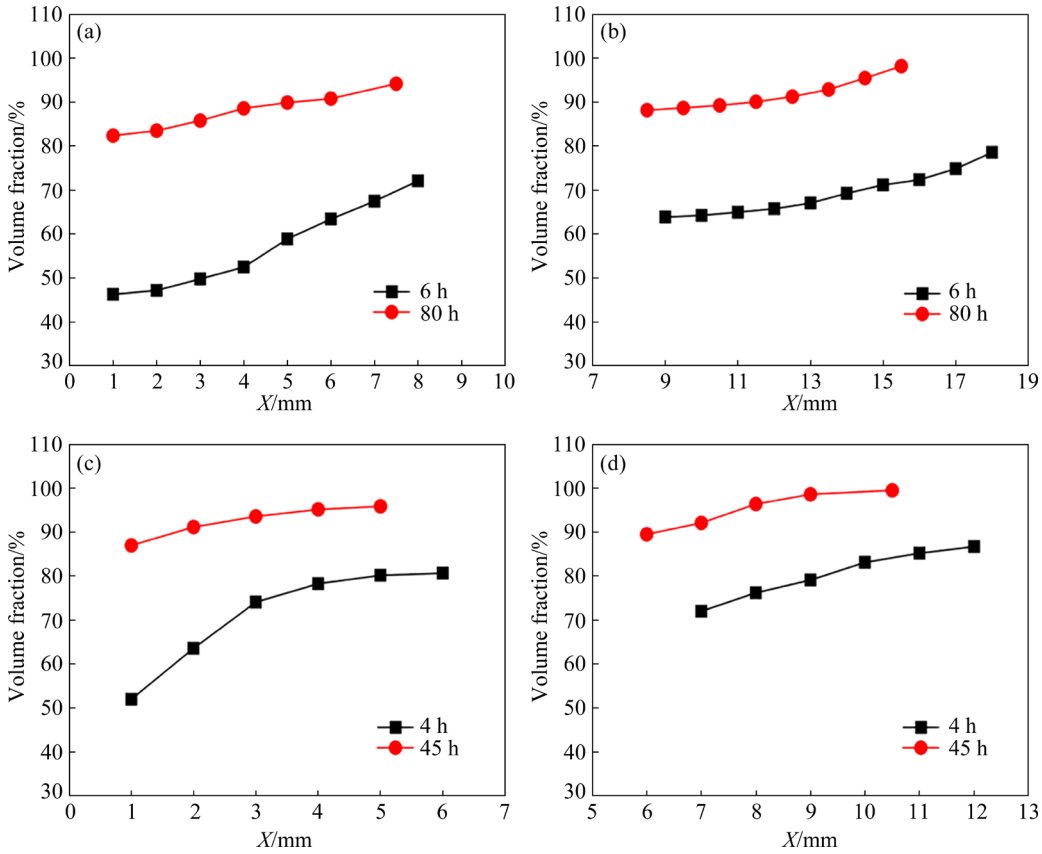

Fig. 3 Dependence of volume fractions of IMCs on position of alloys after different thermal stabilization time: (a, b) Primary and peritectic mushy zones of Sn−9Co alloy, respectively; (c, d) Primary and peritectic mushy zones of Sn−50Cu alloy, respectively

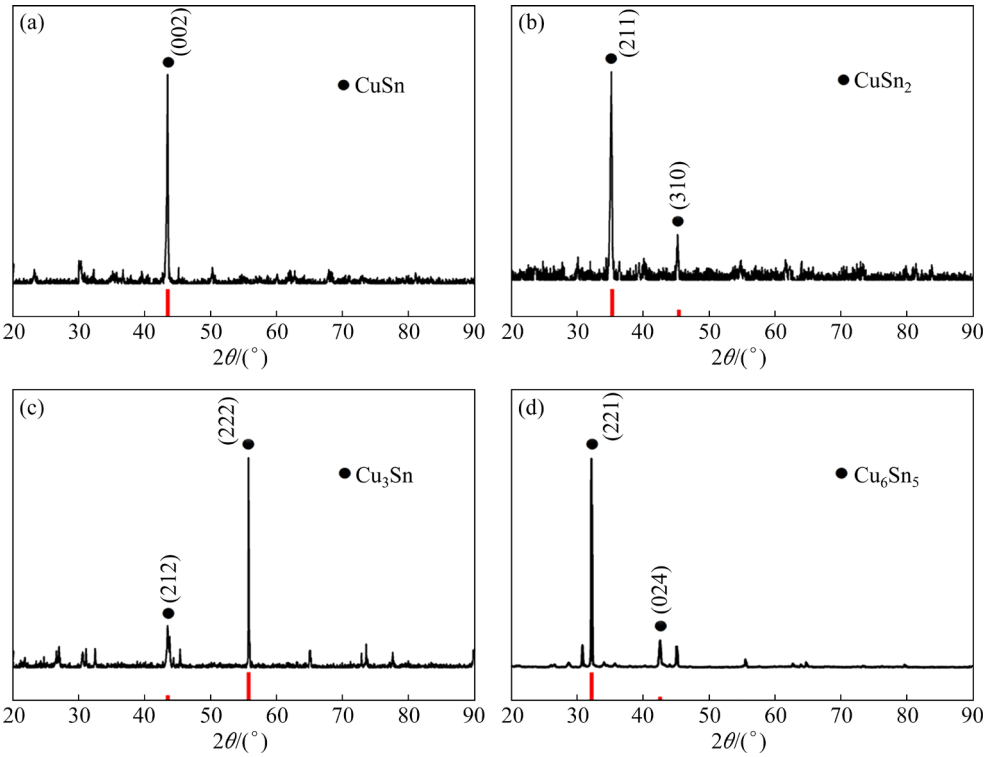

Fig. 4 XRD patterns of different mushy zones of both alloys after long-term thermal stabilization: (a) Primary mushy zone of Sn−9Co alloy at 80 h; (b) Peritectic mushy zone of Sn−9Co alloy at 80 h; (c) Primary mushy zone of Sn−50Cu alloy at 45 h; (d) Peritectic mushy zone of Sn−50Cu alloy at 45 h

corresponding independent elastic coefficient was calculated. Finally, the Young's modulus was calculated from the independent elastic coefficients. The independent elastic coefficients mentioned above are related to the crystal structure of the material, which should be previously specified to determine the corresponding independent elastic coefficient. Further, the value of the sound velocity was determined, and then the light path was set up for the BLS test.

The microscopic anisotropy of the CoSn, $CoSn_2$, Cu_3Sn, and Cu_6Sn_5 phases in the Sn−9Co and Sn−50Cu alloys was also considered. The CoSn and Cu_6Sn_5 phases have hexagonal structures, the $CoSn_2$ phase has a tetragonal structure, and the Cu_3Sn phase has a monoclinic structure [48,49]. Phases with hexagonal and quadrilateral structures require six elastic coefficients, and phases with monoclinic structures require thirteen elastic coefficients. However, the grain orientations in Sn−9Co and Sn−50Cu peritectic alloys were concentrated near one or some of the orientation positions, showing a texture [50]. Therefore, for the CoSn, $CoSn_2$, Cu_3Sn, and Cu_6Sn_5 bulk single-phases, the value of independent elastic coefficients could not be determined by the microscopic anisotropy resulting from the crystal structure. Therefore, it should be determined by the macroscopic anisotropy resulting from the texture phenomenon [51]. In summary, the BLS experiments of the CoSn, $CoSn_2$, Cu_3Sn, and Cu_6Sn_5 phases were not related to their crystal structures.

If these four intermetallic compounds are continuous media, the light path settings for Brillouin light scattering experiments should be based on the following independent elastic coefficients: C_{11}, C_{12}, C_{13}, C_{33}, C_{44}, and C_{66} [51]. To obtain these six independent elastic coefficients, two light paths in the radial and axial directions are required during experiments. BLS experiments under these two light paths were carried out to collect Brillouin spectra by adjusting the incident angle with a fixed sample position. This means that the incident angle for Brillouin light scattering was 10° in the radial light path and 60° in the axial light path when the sample position was constant. In addition, during the BLS experiments on opaque bulk metal samples, diffuse reflection is more likely to occur. The degree of diffuse reflection increases significantly upon increasing the incident angle and causes a weaker phonon signal in the Brillouin spectrum. In summary, the axial light path is not suitable for Brillouin light scattering experiments on bulk metallic samples. Therefore, the vertical and horizontal samples of CoSn, $CoSn_2$, Cu_3Sn, and Cu_6Sn_5 phases were prepared, and the minimum value of 10° of the adjustable angle was used as the incident angle to collect the Brillouin spectra. Diffuse reflection during the experiment was minimized, providing clear and accurate phonon signals. In conclusion, the horizontal and vertical samples of the IMCs prepared in this work were unrelated to the crystal structure and were based only on the light path setting. Figures 5(a−d) show the BLS spectra of these IMCs, where the black and red curves present the measurement results of the vertical and horizontal samples, respectively.

According to the BLS results, the instrument can receive two kinds of signals. The first signal is the reference light entering directly from the laser, which corresponds to the reference peak with no frequency shift in its spectrum. The second signal is the elastic wave propagating along the wave vector direction on the sample surface, which corresponds to the negative-frequency Stokes peak and the positive-frequency anti-Stokes peak [44]. The peak position represents the change in the frequency of incident light after inelastic scattering, i.e., the frequency shift. The blue dotted lines mark the bulk phonon spectral peak of the measured sample, and the longitudinal acoustic wave and the transverse acoustic wave are marked as L and T, respectively. The main laser peak was strongly attenuated relative to the secondary peak, so a Brillouin spectrum measured in the presence of a strong elastic component will inevitably show these secondary peaks in the background spectrum.

The corresponding frequency shifts of the transverse and longitudinal waves are given in Table 1, where f_{RV} and f_{RH} are the rayleigh wave frequency shifts of vertical and horizontal samples, respectively; f_{LH} and f_{TH} are the frequency shifts of longitudinal wave and transverse wave measured with horizontal samples, respectively; f_{LV} and f_{TV} are the frequency shifts of longitudinal wave and transverse wave measured with vertical samples, respectively.

According to the BLS selection rule for opaque materials, the signal peaks of quasi-longitudinal mode (L) and pure-transverse mode 1

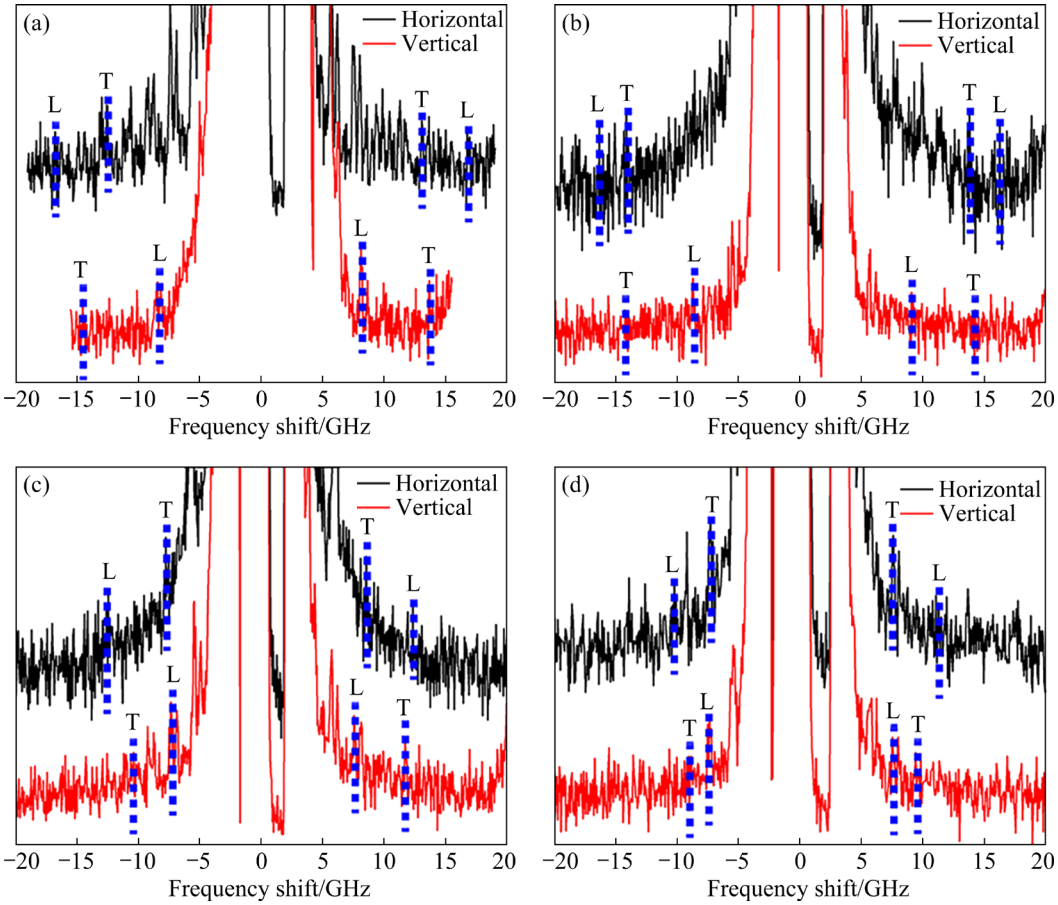

Fig. 5 BLS spectra of four intermetallic compounds on vertical and horizontal samples: (a) CoSn phase; (b) $CoSn_2$ phase; (c) Cu_3Sn phase; (d) Cu_6Sn_5 phase

Table 1 Frequency shifts of transverse and longitudinal waves

Intermetallic compound	f_{RV}/ GHz	f_{RH}/ GHz	f_{LV}/ GHz	f_{TV}/ GHz	f_{LH}/ GHz	f_{TH}/ GHz
CoSn	5.4	3.9	16.7	14.4	8.2	13.8
$CoSn_2$	5.4	3.75	16.3	13.8	8.7	14.2
Cu_3Sn	5.6	5.7	12.8	7.8	7.5	10.7
Cu_6Sn_5	5.6	5.5	10.2	7.5	7.3	9.3

(T_1) can be obtained in the symmetric scattering geometry setting. The signal peaks of quasi-longitudinal mode, pure-transverse mode 1, and pure-transverse mode 2 (T_2) can be obtained in the backscattering geometry setting [52]. In this work, the 180° backscattering setting was chosen to obtain the signal peaks in the Brillouin spectra for the quasi-longitudinal mode, pure-transverse mode 1, and pure-transverse mode 2 according to the selection rule. For Brillouin spectra of bulk alloys, the signal peak distribution from low to high frequencies usually follows the order: pure-transverse mode 1, quasi-longitudinal mode, and pure-transverse mode 2. The signal of pure transverse mode 2 has the weakest intensity compared with the other modes within the same spectrum. In addition, the BLS experiment on an opaque bulk sample cannot completely detect the signal peaks of these three modes in most conditions.

The longitudinal and transverse modes mentioned above correspond to the longitudinal and transverse acoustic waves in this work. The Brillouin spectra shown in Fig. 5 were obtained by Lorentzian fitting to determine the frequency shifts of the Rayleigh surface wave and longitudinal acoustic wave for the vertical and horizontal samples of these four IMCs. Based on the selection rule and the distribution of the signal peaks, the signal peaks collected during the BLS experiments for vertical samples of the IMCs were in the quasi-longitudinal mode and the pure-transverse mode 1. For horizontal samples, the signal peaks

were collected in quasi-longitudinal mode and pure-transverse mode 2. Because only one transverse mode was collected in both the horizontal and vertical samples, the transverse acoustic waves were not marked as T_1 and T_2 respectively, and were simply marked by T in Fig. 5. Therefore, the high-frequency mode was transverse mode, while the low-frequency mode was the longitudinal mode in the horizontal samples of these four IMCs.

4.3 Calculation results and analysis of Young's modulus

According to conservation of momentum, the magnitude of wave vector (q_B) of the BAW can be expressed as [45]

$$\left|q_B\right|=\frac{4\pi n}{\lambda}\sin\left(\frac{\varphi}{2}\right) \tag{2}$$

where n is the refractive index, λ is the wavelength of the incident light, and φ is the angle between the incident light and scattered light. For the backscattering configuration, φ=180°, so the corresponding magnitude of phonon wave vector is [43]

$$\left|q_B\right|=\frac{4\pi n}{\lambda} \tag{3}$$

According to the conservation of in-plane momentum, the magnitude of the wave vector of RSAW is [53]

$$\left|q_R\right|=\frac{4\pi\sin\theta_i}{\lambda} \tag{4}$$

where θ_i is the incident angle. The dispersion relation of the acoustic phonon is linear, and the sound velocity for BAW (v_B) and RSAW (v_R) corresponds to the slope of the dispersion relation as follows [54]:

$$v_B=\frac{2\pi f}{q_B} \tag{5}$$

$$v_R=f/q_R \tag{6}$$

where f is the frequency shift.

For BAW and RSAW, the sound velocities expressions are [53]

$$v_B=\frac{\lambda f_{BAW}}{2n} \tag{7}$$

$$v_R=\frac{\lambda f_{RSAW}}{4\pi\sin\theta_i} \tag{8}$$

where f_{BAW} and f_{RSAW} are the frequency shifts of bulk acoustic waves and rayleigh surface acoustic waves, respectively.

The RSAW and longitudinal wave of IMCs were obtained by Lorentzian fitting. The frequency shift of these two waves was substituted into the above formula to obtain the respective Rayleigh wave velocity v_R and longitudinal wave velocity (v_T). Relationship between v_R and v_B is [18]

$$4v_T^3\left(v_L^2-v_R^2\right)^{1/2}\left(v_T^2-v_R^2\right)^{1/2}=v_L\left(2v_T^2-v_R^2\right)^2 \tag{9}$$

The transverse wave velocity v_L can be obtained. Since the RSAW peak is strong and sharp, while the BAW peak is weak and miscellaneous, in order to make the BAW clear, only the BAW is shown in the spectra, and no complete RSAW is shown. The results for sound velocity calculation of IMCs and the parameters used in the calculation are shown in Table 2.

For the four intermetallic compounds as the continuous media, CoSn, $CoSn_2$, Cu_3Sn and Cu_6Sn_5, the independent elastic coefficient matrix is as follows [51]:

$$\boldsymbol{C}_{ij}=\begin{bmatrix} C_{11} & C_{12} & C_{13} & 0 & 0 & 0 \\ C_{12} & C_{11} & C_{13} & 0 & 0 & 0 \\ C_{13} & C_{13} & C_{33} & 0 & 0 & 0 \\ 0 & 0 & 0 & C_{44} & 0 & 0 \\ 0 & 0 & 0 & 0 & C_{44} & 0 \\ 0 & 0 & 0 & 0 & 0 & C_{66} \end{bmatrix} \tag{10}$$

The relationship between the elastic coefficient and sound velocity is established by the following

Table 2 Physical parameters and partial calculation results of IMCs

Intermetallic compound	λ/nm	ρ/(g·cm^{-3})	n	v_{RV}/(m·s^{-1})	v_{RH}/(m·s^{-1})	v_{LV}/(m·s^{-1})	v_{TV}/(m·s^{-1})	v_{LH}/(m·s^{-1})	v_{TH}/(m·s^{-1})
CoSn	532	8.09	2.19	1345.5	971.7	2019.2	1741.1	991.5	1668.5
$CoSn_2$	532	7.82	2.19	1345.5	934.3	1970.8	1668.5	1051.9	1716.9
Cu_3Sn	532	9.03 [55]	1.18	1395.3	1420.2	2885.4	1758.3	1690	2417
Cu_6Sn_5	532	8.19 [55]	1.18	1395.3	1370.4	2299.3	1690.7	1645.6	2096.4

formulas [51]:

$$C_{11} = \rho v_{LH}^2 \quad (11)$$

$$C_{33} = \rho v_{LV}^2 \quad (12)$$

$$C_{44} = \rho v_{TV}^2 \quad (13)$$

$$C_{66} = \rho v_{TH}^2 \quad (14)$$

$$C_{12}=C_{11}-2C_{66} \quad (15)$$

$$C_{13}=C_{33}-2C_{44} \quad (16)$$

where v_{LH} and v_{TH} are the longitudinal and transverse wave velocities measured with horizontal samples, respectively; v_{LV} and v_{TV} are the longitudinal and transverse wave velocities measured for vertical samples, respectively. After all the independent elastic coefficients were obtained, the Young's modulus E was calculated separately using the following equation [54]:

$$E = \frac{(C_{11}-C_{12})\left[C_{33}(C_{11}+C_{12})-2C_{13}^2\right]}{C_{11}C_{33}-C_{13}^2} \quad (17)$$

The independent elastic coefficient matrices and Young's moduli of the four intermetallic compounds obtained through the BLS method are presented in Table 3. The calculated Young's moduli of CoSn, $CoSn_2$, Cu_3Sn, and Cu_6Sn_5 phases are 115.0, 101.7, 129.9, and 125.6 GPa, respectively, which are in good agreement with the previous experimental results. However, the Young's moduli in this experiment are slightly lower than those obtained using nanoindentation in most references. In the nanoindentation experiments, when the indenter is pressed into a sample, the dislocations expand into the sample under the action of the indenter's stress field. This, in turn, causes plastic deformation and strengthening within the sample, leading to an overestimation of the Young's modulus. Because BLS is a non-destructive measurement technique, when combined with the better single-phase samples of IMCs and appropriate calculation methods, the Young's moduli obtained by the BLS method are expected to be more accurate.

Table 3 Young's moduli and independent elastic coefficients of four intermetallic compounds

Intermetallic compound	C_{11}	C_{12}	C_{13}	C_{33}	C_{44}	C_{66}	E/GPa
CoSn	33	−16	37.1	7.9	22.5	24.5	115.0
$CoSn_2$	30.4	−13.2	−37.5	8.7	21.8	21.8	101.7
Cu_3Sn	75	19.2	−79.5	25.8	52.7	27.9	129.9
Cu_6Sn_5	43.3	−3.5	−49.8	22.2	36	23.4	125.6

5 Conclusions

(1) The single-phase regions of CoSn, $CoSn_2$, Cu_3Sn, and Cu_6Sn_5 phases required for the BLS test were obtained by applying long-term thermal stabilization. The volume fractions of these four intermetallic compound phases near the solid−liquid interface were 98.3%, 94.2%, 99.6%, and 95.9%, respectively.

(2) All of the independent elastic coefficients and Young's moduli of CoSn, $CoSn_2$, Cu_3Sn, and Cu_6Sn_5 phases were obtained by performing Brillouin light scattering experiments on both the horizontal and vertical samples of these phases. The calculated Young's modului of the about phases were 115.0, 101.7, 129.9, and 125.6 GPa, which demonstrates the effectiveness of Brillouin light scattering for measuring the Young's modulus of IMCs in bulk alloys.

(3) The Young's modulus measured by the Brillouin light scattering method was slightly lower than that obtained by the nanoindentation. The overestimation of Young's modulus was caused by different degrees of plastic deformation during the nanoindentation experiment. Therefore, it is important to explore the non-contact Brillouin light scattering method to measure Young's modulus of materials.

CRediT authorship contribution statement

Peng PENG: Conceptualization, Formal analysis, Funding acquisition, Writing − Original draft, Writing − Review and editing; **Lin LIU:** Supervision, Investigation; **Lu GAN** and **Yang-xin YU:** Data curation, Formal analysis, Writing − Original draft, Writing − Review and editing; **Yuan-li XU**, **Xu-dong ZHANG** and **Zhi−kun MA:** Investigation; **Guo-zhi CHAI:** Resources, Data curation.

Declaration of competing interest

The authors declare that they have no known competing financial interests or personal relationships that could have appeared to influence the work reported in this paper.

Acknowledgments

This study was supported by the Gansu Key Research and Development Project, China (No. 23YFGA0003), the Key Science and Technology Projects of Gansu Province, China (No. 22ZD6GB019), Gansu Provincial Joint Research Fund, China (No. 23JRRC0004), the Industry Support Plan of Gansu Universities, China (No. 2024CYZC-01), and the Fundamental Research Funds for the Central Universities, China (No. lzujbky-2022-ey15).

Supplementary Materials

Supplementary Materials in this paper can be found at: http://tnmsc.csu.edu.cn/download/16-p3030-2024-0018-Supplementary_Materials.pdf.

References

[1] KIM S, KIM H, KIM N J. Brittle intermetallic compound makes ultrastrong low-density steel with large ductility [J]. Nature, 2015, 518: 77−79.

[2] THIYANESHWARAN N, SELVAN C P, LAKSHMI-KANTHAN A, SIVAPRASAD K, RAVISANKAR B. Comparison based on specific strength and density of in-situ Ti/Al and Ti/Ni metal intermetallic laminates [J]. Journal of Materials Research and Technology, 2021, 14: 1126−1136.

[3] JIANG Yao, HE Yue-hui, GAO Hai-yan. Recent progress in porous intermetallics: Synthesis mechanism, pore structure, and material properties [J]. Journal of Materials Science & Technology, 2021, 74: 89−104.

[4] LIU Zhe-dong, YANG Jie-ren, CHENG Rui-run, DU Zhao-xin. Ti_2AlNb-based intermetallic compounds: Research progress, challenges and prospects [J]. Transactions of Nonferrous Metals Society of China, 2023, 33(12): 4039−4058.

[5] WANG Gang, CAI Ying-jun, XU Qi-ming, ZHOU Cong, TAN Cai-wang, CAO Wei. Microstructural and mechanical properties of inconel 600/ZrB_2−SiC joints brazed with AgCu/Cu-foam/AgCu/Ti multi-layered composite filler [J]. Journal of Materials Research and Technology, 2020, 9: 3430−3437.

[6] OZAN S, LIN Ji-xing, ZHANG Yao-wu, LI Yun-cang, WEN Cui. Cold rolling deformation and annealing behavior of a β-type Ti−34Nb−25Zr titanium alloy for biomedical applications [J]. Journal of Materials Research and Technology, 2020, 9: 2308−2318.

[7] AKMAL M, SEONG H, RYU H. Mo and Ta addition in NbTiZr medium entropy alloy to overcome tensile yield strength−ductility trade-off [J]. Journal of Materials Science & Technology, 2022, 109: 176−185.

[8] WANG Dong, HE Guo, TIAN Ye, REN Ning, NI Jia-hua, LIU Wei, ZHANG Xian-long. Evaluation of channel-like porous-structured titanium in mechanical properties and osseointegration [J]. Journal of Materials Science & Technology, 2020, 44: 160−170.

[9] KAPLANSKII Y, ZAITSEV A, SENTYURINA Z, LEVASHOV E, POGOZHEV Y, LOGINOV P, LOGACHEV I. The structure and properties of pre-alloyed NiAl−Cr(Co,Hf) spherical powders produced by plasma rotating electrode processing for additive manufacturing [J]. Journal of Materials Research and Technology, 2018, 7: 461−468.

[10] AI Cheng, ZHAO Xin-bo, CHEN Xi, GUO Min, HUANG Tai-wen, LIU Lin. Effect of Hf content on microstructure and friction properties of $CoCrFeNiHf_x$ eutectic high entropy alloy [J]. Transactions of Nonferrous Metals Society of China, 2023, 33(9): 2850−2860.

[11] CAO Guo-xin, GAO Hua-jian. Mechanical properties characterization of two-dimensional materials via nano-indentation experiments [J]. Progress in Materials Science, 2019, 103: 558−595.

[12] HOLANDA J, MAIOR D S, AZEVEDO A, REZENDE S M. Detecting the phonon spin in magnon−phonon conversion experiments [J]. Nature Physics, 2018, 14: 500−506.

[13] YANG Jian-yan, REN Wei-jun, ZHAO Xin-guo, KIKUCHI T, MIAO Ping, NAKAJIMA K, LI Bing, ZHANG Zhi-dong. Mictomagnetism and suppressed thermal conduction of the prototype high-entropy alloy CrMnFeCoNi [J]. Journal of Materials Science & Technology, 2022, 99: 55−60.

[14] FILLON A, JAOUEN C, MICHEL A, ABADIAS G, TROMAS C, BELLIARD L, PERRIN B, DJEMIA P. Lattice instability and elastic response of metastable $Mo_{1-x}Si_x$ thin films [J]. Physical Review B, 2013, 88: 174104.

[15] RAHAMAN M M, KOJIMA S. Brillouin scattering study of electro-optic $KTa_{1-x}Nb_xO_3$ crystals [J]. Materials, 2023, 16: 652.

[16] SINGARAJU A B, BAHL D, STEVENS L L. Brillouin light scattering: Development of a near century-old technique for characterizing the mechanical properties of materials [J]. AAPS PharmSciTech, 2019, 20: 109.

[17] APREUTESEI M, DJEMIA P, BELLIARD L, ABADIAS G, ESNOUF C, BILLARD A, STEYER P. Structural-elastic relationships of Zr−TL (TL=Cu,Co,Ni) thin films metallic glasses [J]. Journal of Alloys and Compounds, 2017, 707: 126−131.

[18] LI Zhao, WU Yong-quan, WANG Sai. Brillouin scattering study on elastic properties of polycrystal metals [J]. Shanghai Metals, 2012, 34: 6−10.

[19] LI Qiang, CHEN Cheng, WANG Ming-ge, LV Yao-hui, MAO Yu-lu, XU Man-zhang, WANG Ying-nan, WANG Xue-wen, ZHANG Zhi-yong, WANG Shou-guo, ZHAO Wu, STIENS J. Study on photoelectricity properties of SiCN thin films prepared by magnetron sputtering [J]. Journal of Materials Research and Technology, 2021, 15: 460−467.

[20] OANH VU T K, TRAN M T, TU N X, BAO N, KIM E K. Electronic transport mechanism and defect states for p-InP/i-InGaAs/n-InP photodiodes [J]. Journal of Materials Research and Technology, 2022, 19: 2742−2749.

[21] DIALLO B, TOPKA K C, PUYO M, LEBESGUE C, GENEVOIS C, LALOO R, SAMELOR D, LECOQ H, ALLIX M, VERGNES H. Network hydration, ordering and composition interplay of chemical vapor deposited amorphous silica films from tetraethyl orthosilicate [J]. Journal of Materials Research and Technology, 2021, 13: 534−547.

[22] WANG Xu, ZHANG Wen, ZHONG Yu-jie, SUN Lu-chao, HU Qiao-dan, WANG Jing-yang. Introduction of low strain

energy $GdAlO_3$ grain boundaries into directionally solidified $Al_2O_3/GdAlO_3$ eutectics [J]. Acta Materialia, 2021, 221: 117355.

[23] LI Xu-guang, LI Shuang-ming, LI Dou, YANG Bin, XU Chang-jiang, ZHONG Hong. Effect of hot pressing on the microstructure and thermoelectric properties of TGZM-grown YbFe-doped $CoSb_3$ skutterudite [J]. Ceramics International, 2021, 47: 8949−8958.

[24] NGUYEN THI H, DREVET B, DEBIERRE J M, CAMEL D, DABO Y, BILLIA B. Preparation of the initial solid−liquid interface and melt in directional solidification [J]. Journal of Crystal Growth, 2003, 253: 539−548.

[25] BÖSENBERG U, BUCHMANN M, RETTENMAYR M. Initial transients during solid/liquid phase transformations in a temperature gradient [J]. Journal of Crystal Growth, 2007, 304: 281−286.

[26] PENG Peng, LI Xin-zhong, LI Jian-gong, SU Yan-qing, GUO Jing-jie, FU Heng-zhi. Influence of solutal convection on solute distribution of melt during preparation of directionally solidified Sn−36at.%Ni peritectic alloy [J]. International Journal of Heat and Mass Transfer, 2015, 84: 73−79.

[27] RETTENMAYR M. Melting and remelting phenomena [J]. International Materials Reviews, 2009, 54: 1−17.

[28] LISCHNER D J, BASSECHES H, D'ALTROY F A. Observations of the temperature gradient zone melting process for isolating small devices [J]. Journal of the Electrochemical Society, 1985, 132(12): 2997−3001.

[29] PFANN W. Temperature gradient zone melting [J]. Transaction of American Institute of Mining, Metallurgical, and Petroleum Engineers, 1955, 203: 961−964.

[30] SALLOUM-ABOU-JAOUDE G, REINHART G, COMBEAU H, ZALOŽNIK M, LAFFORD T A, NGUYEN-THI H. Quantitative analysis by in situ synchrotron X-ray radiography of the evolution of the mushy zone in a fixed temperature gradient [J]. Journal of Crystal Growth, 2015, 411: 88−95.

[31] PHILLION A B, ZALOŽNIK M, SPINDLER I, PINTER N, ALEDO C A, SALLOUM-ABOU-JAOUDE G, NGUYEN THI H, REINHART G, BOUSSINOT G, APEL M, COMBEAU H. Evolution of a mushy zone in a static temperature gradient using a volume average approach [J]. Acta Materialia, 2017, 141: 206−216.

[32] PAN Shi-yan, ZHANG Qing-yu, ZHU Ming-fang, RETTENMAYR M. Liquid droplet migration under static and dynamic conditions: Analytical model, phase-field simulation and experiment [J]. Acta Materialia, 2015, 86: 229−239.

[33] LÖFFLER A, REUTHER K, ENGELHARDT H, LIU D M, RETTENMAYR M. Resolidification of the mushy zone of multiphase and multicomponent alloys in a temperature gradient-Experiments and modeling [J]. Acta Materialia, 2015, 911: 34−40.

[34] PAWAR S, WANG K, YECKEL A, DERBY J. Analysis of temperature gradient zone melting and the thermal migration of liquid particles through a solid [J]. Acta Materialia, 2022, 228: 117780.

[35] WANG Hong-qiang, LI Shuang-ming, LI Xin, ZHONG Hong. Microstructure and thermoelectric properties of doped p-type $CoSb_3$ under TGZM effect [J]. Journal of Crystal Growth, 2017, 466: 56−63.

[36] CHEN Bai-shan, HUANG Yu-feng, TANG Si-wei, LIU Wen-sheng, MA Yun-zhu. Tuning the microstructure and enhancing the mechanical properties of Au−20Sn/Au/Ni(P)/Kovar joint by ultrasonic-assisted soldering method [J]. Journal of Materials Research and Technology, 2021, 14: 703−718.

[37] ZHAO Jiong-fei, LI Ming-xing, WANG Hai-peng, WEI Bing-bo. A kinetic transition from peritectic crystallization to amorphous solidification of rapidly quenched refractory Nb−Ni alloy [J]. Acta Materialia, 2022, 237: 118127.

[38] SANDERCOCK J R. Brillouin scattering study of SbSi using a double-passed, stabilised scanning interferometer [J]. Optics Communications, 1970, 2: 73−76.

[39] HILLEBRANDS B, MOCK J R, SANDERCOCK R. Construction and performance of a Brillouin scattering set-up using a triple-pass tandem Fabry-Perot interferometer [J]. Journal of Physics E: Scientific Instruments, 1987, 20: 656−659.

[40] SANDERCOCK J R. Trends in Brillouin scattering: Studies of opaque materials, supported films, and central modes [M]. Heidelberg: Springer, 1982.

[41] KEARNS K, STILL T, FYTAS G, EDIGER M. High-modulus organic glasses prepared by physical vapor deposition [J]. Advanced Materials, 2010, 22: 39−42.

[42] OLSSON K S, KLIMOVICH N, AN K, SULLIVAN S, WEATHERS A, LI Shi, LI Xiao-qin. Temperature dependence of Brillouin light scattering spectra of acoustic phonons in silicon [J]. Applied Physics Letters, 2015, 106: 051906.

[43] HASHIMOTO K Y. Surface acoustic wave devices in telecommunications: Modelling and simulation [M]. Heidelberg: Springer, 2000.

[44] XIE Ya-ru, REN Shu-liang, GAO Yuan-fei, LIU Xue-lu, TAN Ping-heng, ZHANG Jun. Measuring bulk and surface acoustic modes in diamond by angle-resolved Brillouin spectroscopy [J]. Science China Physics, Mechanics & Astronomy, 2021, 64: 287311.

[45] PALOMBO F, FIORETTO D. Brillouin light scattering: Applications in biomedical sciences [J]. Chemical Reviews 2019, 119: 7833−7847.

[46] LEE J, KO J, ROLEDER K, RYTZ D. Complete determination of elastic stiffness coefficients and local symmetry breaking in the paraelectric barium titanate [J]. Applied Physics Letters, 2019, 114: 072901.

[47] SALZENSTEIN P, THOMAS Y W. Uncertainty estimation for the Brillouin frequency shift measurement using a scanning tandem Fabry–Pérot interferometer [J]. Micromachines, 2023, 14: 1429.

[48] CHEN Jiunn, LI Yi-shao, YANG Ping-feng, REN Chung-yuan, HUANG Di-jing. Structural and elastic properties of Cu_6Sn_5 and Cu_3Sn from first-principles calculations [J]. Journal of Materials Research, 2009, 24: 2361−2372.

[49] LIU Jin-ming, ZHAI Wen, WANG Ben-ju, MA Xu, YAN Peng-xun, WEI Bing-bo. Structure and property modulation of primary CoSn and peritectic $CoSn_2$ intermetallic compounds through ultrasonicating liquid Sn−10%Co alloy

[J]. Journal of Alloys and Compounds, 2020, 27: 154297.
[50] KARTHIK M, JAN J, MADIKKAMADOM R, KARTHIK V, SUDARSANAN A. Titanium in cast Cu−Sn alloys — A review [J]. Materials, 2021, 14: 4587.
[51] KOSKI K J, AKHENBLIT P, MCKIERNAN K, YARGER J I. Non-invasive determination of the complete elastic moduli of spider silks [J]. Nature Materials, 2013, 12: 262−267.
[52] WANG Sai, WU Yong-quan, ZHOU Guo-zhi, LI Zhao, MENG Wen-jian. Brillouin Scattering investigation of single-crystal aluminum nitride [J]. Journal of Light Scattering, 2013, 25: 138−141.
[53] PANG Si-min, XIE Ya-ru, ZHANG Jun. Review of investigating the elastic and thermal properties by angle-resolved Brillouin light scattering [J]. Journal of Light Scattering, 2021, 33: 101−111.
[54] CUSACK S, MILLER A. Determination of the elastic constants of collagen by Brillouin light scattering [J]. Journal of Molecular Biology, 1979, 135: 39−51.
[55] XIAN J W, ZENG G, BELYAKOV S A, GU Q, NOGITA K, GOURLAY C M. Anisotropic thermal expansion of Ni_3Sn_4, Ag_3Sn, Cu_3Sn, Cu_6Sn_5 and β Sn [J]. Intermetallics, 2017, 91: 50−64.

通过布里渊光散射无损测量金属间化合物相的杨氏模量

彭 鹏[1]，刘 林[2]，甘 露[3]，喻杨新[1]，徐远丽[1]，张旭东[1]，马智锟[1]，柴国志[4]

1. 兰州大学 材料与能源学院，兰州 730000；
2. 西北工业大学 凝固技术全国重点实验室，西安 710072；
3. 兰州金川科技园区有限公司，兰州 730101；
4. 兰州大学 物理科学与技术学院，兰州 730000

摘 要：与目前金属材料杨氏模量的测量方法不同，本文采用基于布里渊光散射(BLS)的无损方法获得金属间化合物(IMCs)的杨氏模量。通过调控温度梯度进行长时间的热稳定处理，获得了 BLS 试验所需的 CoSn、$CoSn_2$、Cu_3Sn 和 Cu_6Sn_5 单相区，样品中接近固液界面处对应相的体积分数分别为 98.3%、94.2%、99.6%和 95.9%。所有 IMC 的独立弹性系数和杨氏模量均通过布里渊散射仪和不同方向样品的 BLS 实验获得。采用本文方法计算得到 CoSn、$CoSn_2$、Cu_3Sn 和 Cu_6Sn_5 相的杨氏模量分别为 115.0、101.7、129.9 和 125.6 GPa，与前人的实验结果吻合较好，证实了 BLS 测量块体合金中 IMCs 杨氏模量的有效性。

关键词：布里渊光散射；金属间化合物；弹性刚度张量；热稳定；杨氏模量

(Edited by Wei-ping CHEN)